




Radiation from Flames in a Microgravity Environment: Experimental and Numerical Investigations

L. Carmignani* , K. Dong and S. Bhattacharjee, Mechanical Engineering Department, San Diego State University, 5500 Campanile Dr, San Diego, CA 92182, USA

Received: 29 October 2018/Accepted: 25 June 2019

Abstract. Fire safety in microgravity is extremely important due to the potential threat of fire for astronauts and spacecraft. One of the main effects of reduced gravity on combustion processes is the suppression of buoyancy. When the flow field around a flame is very mild, radiative exchanges between flame, solid fuel, and environment can determine the flame strength and growth. During the recent Burning and Suppression of Solid Fuels (BASS) investigation, several thin flat acrylic samples were burned in opposed-flow configuration with flow velocity varying between 0 cm/s and 42 cm/s, thicknesses from 100 μm to 400 μm , and oxygen concentration between 17% and 22%. Total radiation recorded by a radiometer positioned at a fixed location with a complete view of the spreading flame is presented as a function of different parameters. The radiometer signal is found to vary strongly with flow velocity, all other conditions unchanged. By processing the experiment videos with a MATLAB image processing code, data on flame length, projected flame area, sooty area (represented by the yellow color as opposed to blue), and burning rate (through evaluation of instantaneous flame spread rate) are obtained to explore if the radiation signature can be correlated with sooty or overall flame areas, or the burning rate. A comprehensive numerical model that includes gas and surface radiation, including radiation feedback from the gas to the solid, but not soot, is used to explore the same parametric study of the BASS flames' total radiation signature. The detailed information obtained from the numerical solutions are used to interpret the radiation measurements in the microgravity experiments, which can be used for testing and refining further modeling efforts.

Keywords: Microgravity flames, Flame radiation, BASS experiments

1. Introduction

Flame spread over thin solid fuels has been studied during the last five decades for the implications on fire safety and understanding of the basic mechanisms of flames [1, 2]. Due to the large variety of factors affecting flame growth and propa-

* Correspondence should be addressed to: L. Carmignani, E-mail: luca.carmignani@icloud.com



gation, researchers often try to isolate the importance of a few variables at a time, such as flow velocity, oxygen concentration, pressure or external heating.

The flow field surrounding the flame is one of the most influential factors in flame spread. Based on flow and flame directions, the problem is defined as concurrent or opposed-flow flame spread, with the latter being considered in this work. The flow velocity determines the availability of the oxidizer in the reaction zone, which is measurable through the residence time (time spent by the oxidizer near the flame). When the time required by the chemical reactions to occur (chemical time) is much smaller than the residence time, the flame is in equilibrium conditions, or the thermal regime [3]. On the other hand, the residence time decreases with higher velocities while variations in the chemical time are negligible. The ratio of the two, defined as the Damkohler number, can decrease below a critical value when the flow intensifies, leading to blow-off extinction (kinetic regime) [4]. In microgravity, the buoyant flow generated by a flame can be almost completely suppressed by reducing the flow velocity to zero. In this case flame reactions are controlled by the oxidizer diffusion, which has a larger characteristic time than convection, and the importance of flame radiation drastically increases despite the small size of the flames (radiative regime) [5]. The characteristic radiation time for gas and solid phases, in fact, becomes comparable to the increased residence time.

The effect of oxygen concentration under a forced flow was investigated by Fernandez-Pello et al. [6], who showed how flame spread rates over flat fuels first increase and then decrease as a function of flow velocity, with the peak values depending on fuel thickness and oxygen level. More recently, Zhao et al. explored the effect of pressure on flame spread rate and flame height for downward spread. By testing PMMA slabs in locations with three different ambient pressures, they measured the increase in flame strength for higher pressures [7].

Oxygen and pressure effects have also been studied in microgravity in the 1990s with the Solid Surface Combustion Experiment (SSCE), where thin cellulosic and PMMA samples were tested in a quiescent environment. Bhattacharjee and Altenkirch [8], and later Ramachandra et al. [9], analyzed the flame spread over thin cellulosic fuels at oxygen levels of 35% and 50%, with pressures of 1 atm, 1.5 atm and 2 atm, to understand the role of gas and surface radiation in the radiative regime. They concluded that the flame leading edge was stable and reached steady conditions, and they noticed that higher oxygen and pressure levels produced brighter flames with the formation and growth of the yellow region of the flame. Despite the high oxygen levels (up to 70% by volume), experiments with thick PMMA samples showed an unstable flame behavior with eventual extinction [10], as captured by numerical results that identified radiation losses as the cause [11]. Conductive losses through the sample holder due to the small sample size (59.9 mm long, 3.18 mm thick and 6.35 mm wide), however, might have played a role in flame extinction.

Many factors contribute to the total flame radiation, e.g. flame area, presence of soot, gas and surface temperatures, pressure, etc. The presence of soot is expected to increase the radiative emission and can be estimated by measuring the yellow region of a flame [12, 13]. Indeed, the central region of the flame contains an excess of fuel and displays high soot concentrations, characterized by a yellow

color, in contrast to the blue color of the region close to the leading edge and outer layer of the flame. The radiative intensity of the yellow region is proportional to the soot volume fraction and flame temperature, whereas in the dim blue region of the flame it is mainly given by luminescing radicals. Although the blue region is harder to detect than the sooty region because of the lower brightness, it can be measured with appropriate camera settings or image processing.

Despite the importance of radiation in microgravity flames, direct measurements of radiation emitted by flames over solid fuels had never been measured before the Burning and Suppression of Solids (BASS) and the following BASS-II investigations onboard the International Space Station (ISS). Several flat samples of PMMA were tested at low flow velocities (0–55 cm/s) and various oxygen levels, while nitrogen mass flow rate, flow speed and hemispherical radiation were recorded. They provided fundamental knowledge on flame spread and flammability limits in microgravity, and the results have been discussed in recent papers to confirm the regimes determined by the Damkohler number [14], the critical conditions for radiative extinction [15], and the importance of the boundary layer and development length [16]. However, the variation of flame geometry (measured by projected area and length) with oxygen concentration, and the total radiation captured by the thermopile sensor have not been described.

Radiation measurements from the new microgravity experiments Saffire have been recently discussed by Urban et al. for solid fuels burning in a concurrent configuration [17]. However, the burning conditions in these experiments were fixed, and their influence on flame radiation is hard to determine. In this work, we present total radiation data gathered from the BASS microgravity experiments as functions of opposed flow velocity, oxygen level, and fuel thickness. With image processing, we explore different flame characteristics such as total flame area (from a top view), yellow region of the flame (the sooty region), and the mass burning rate (obtained from the instantaneous flame spread rate) to explain the observed behavior of the emitted radiation. The experimental variables are reproduced in a comprehensive numerical model, which excludes soot radiation, to further explore the dependence of total radiation on the burning conditions.

2. Microgravity Experiments and Video Analysis

The hardware used for the BASS experiments has been described in previous works [18, 19]. It consists of a squared-duct wind tunnel with an internal section of 7.6 by 7.6 cm, placed in the Microgravity Science Glovebox onboard the ISS. A schematic of the BASS set-up is given in Fig. 1. A sample holder like the one shown in the inset of Fig. 1 was mounted on the median plane of the tunnel. A fan on the right side of the tunnel created a forced flow, whose velocity was measured by an omnidirectional spherical air velocity transducer (TSI 8475). A thermopile detector (Oriel 71768, spectral range of 0.13–11 μm), positioned on the top wall, makes an angle of approximately 20° with the middle of the sample and captures the total radiation from the spreading flame. The radiometer was not calibrated against black body emission; nevertheless, its signal can be assumed to be

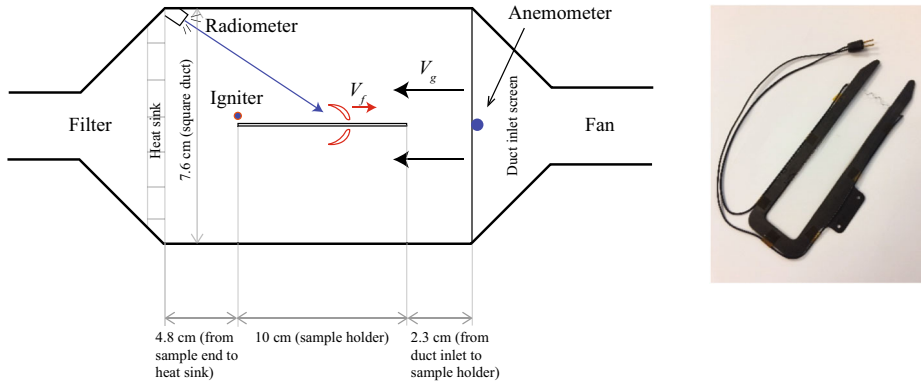


Figure 1. Experimental set-up of the BASS investigation (left) and sample holder (right).

proportional to the total hemispherical radiation received, most of which is controlled by the flame and the burning fuel surface. The time response of the sensor has a delay of a few seconds.

Twenty-two flat samples of PMMA, each about 100 mm long, were tested with varying flow velocity (0–42 cm/s), oxygen concentration (15–22.2%), sample thickness (100–400 μm), and width (1 and 2 cm). Pressure is held constant at 101 kPa. On the left end of the sample, a Kanthal wire was powered for 5–10 s to ignite the samples. A Panasonic camera WV-CP654 with a resolution of 760×480 pixels recorded the experiments from the side of the duct by using a mirror, while still pictures (4320×2968 pixels) from the top of the duct were taken with a Nikon D300 s (equipped with a CMOS sensor, 23.6×15.8 mm, and a 35 mm $f/2.0$ lens), about every 1 s. Values of the radiometer signal, measured flow velocity, and fan power were superimposed on the experiment videos and could be associated to the flame positions.

Side videos and high-resolution still pictures were analyzed using the Flame Image Analysis Tool (FIAT), a MATLAB-based image analysis code publicly available on flame.sdsu.edu. A detailed explanation of the concepts behind FIAT can be found elsewhere [20]. The code can extract the position of the flame in each frame of the video, as well as flame length and area. By considering a still picture of a flame, such as in Fig. 2a, the user can analyze the flame in two ways: (1) intensity tracking and (2) area or color tracking. With the first method, FIAT transforms the flame image from the RGB to the YCrCb color space, where Y is the luminance intensity and Cr and Cb the chrominance channels, and then averages the Y intensity along the direction perpendicular to the flame, creating a two-dimensional image as in Fig. 2b. The part of the image covered by the flame is much brighter than the background, and by choosing appropriate threshold values for the luminance intensity Y, flame leading and trailing edges can be defined as illustrated by the white vertical lines in Fig. 2b. By subtracting the two locations, the flame length can be calculated. FIAT can also be used to measure the area of a flame by using the second method: the area tracking. With this method, frames

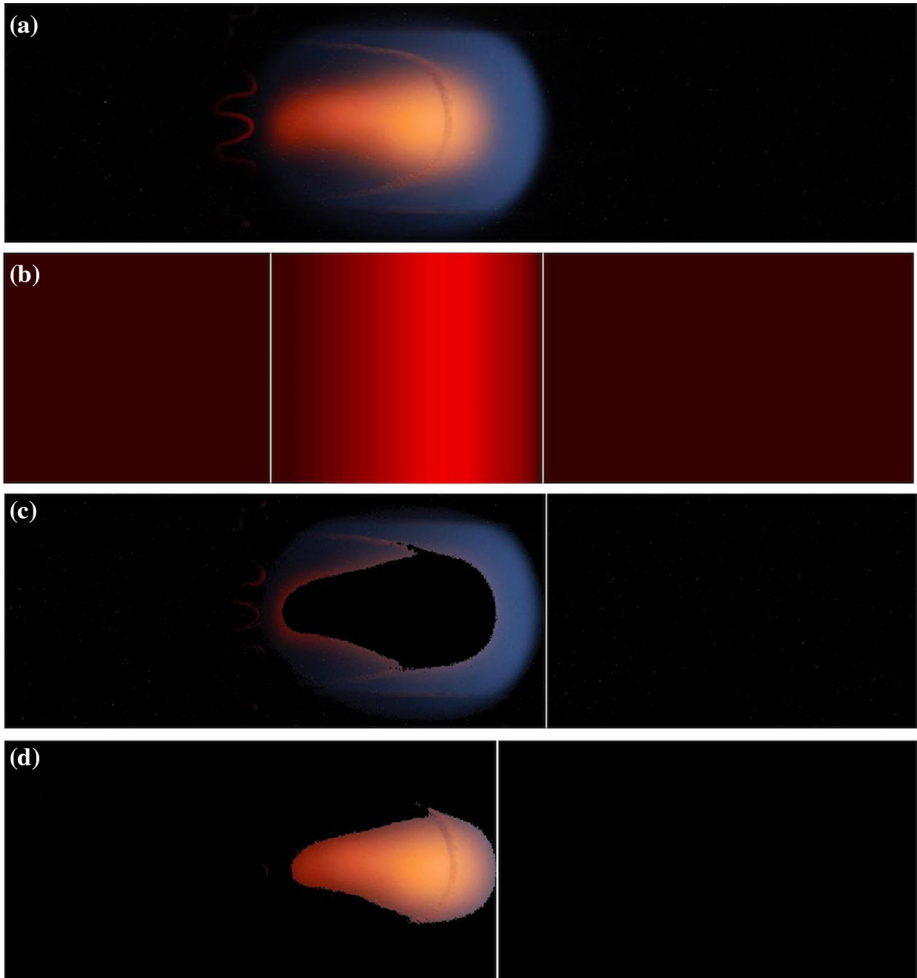


Figure 2. Example of FIAT capabilities. Starting from (a) the original flame, the code averages the luminance intensity in the vertical direction and creates (b) a 2D image, where flame leading and trailing edges can be identified. By using color filtering in the RGB space, (c) the blue region or (d) the sooty area of the flame can be measured and tracked (Color figure online).

are kept in the RGB color space and minimum and maximum values (represented in 8-bit, with values from 0 to 255) are chosen for each color channel. By excluding the points outside of the color-channel intervals, characteristic parts of the flame such as the blue region (Fig. 2c) and yellow sooty part (Fig. 2d) can be isolated and measured. The area tracking method also provides the flame leading edge position as the first point of the flame region in the spreading direction. By

repeating the process for each frame, the evolution in time of flame length and flame area are obtained, as well as flame position and spread rate.

2.1. Numerical Model

The computational model consists of a computational fluids dynamics (CFD) model and a radiation model. In steady-state, the solid fuel approaches the flame with a velocity equal to the spread rate V_f , while the opposed-flow faces the flame with $V_f + V_g$, where V_g is the forced flow velocity.

The locally developed CFD code separately solves gas-phase (2D, laminar, steady-state, x and y momentum, chemical species, and energy) and solid-phase (mass and energy conservation) equations with flame spread rate being the eigenvalue of the problem. More details are available elsewhere [21]. Iterations between gas and solid phase solutions (each providing boundary conditions to the other) continue until the spread rate converges to a value that freezes the flame at a fixed distance from an arbitrarily defined anchor point within the domain. A single-step complete reaction between the fuel and oxidizer with Arrhenius chemical kinetics is used in the gas phase, and a single-step Arrhenius pyrolysis kinetics is used in the solid. Both gas and solid radiation including radiation feedback are included in the model. A constant total emissivity of the fuel surface and the thin-gas approximation in the gas phase are used to simplify the model. However, the Planck mean absorption coefficient a_P is calculated by equating the total emission from a box around the flame using narrow-band radiation solver RADCAL [22] and the thin-gas approximation. RADCAL is also used to solve for the radiative fluxes for each band according to:

$$\dot{q}''_{\lambda} = \int i'_{\lambda} d\Omega \quad (1)$$

The integral of i'_{λ} , which represents the line-of-sight radiation intensity for a given wavelength, over the solid angle $d\Omega$ is evaluated considering the finite width of the flame, therefore including the three-dimensionality of a flame. More details about the radiation model are available in Bhattacharjee et al. [23].

The radiation solver is separated from the CFD solver and a_P , along with the radiative flux contributions, are updated in a nested iteration scheme. A CPU time on the order of one to several hours is required for convergence.

The domain of the numerical simulation is divided into a non-uniform grid structure of 360×120 , corresponding to almost twice the experimental domain. The temperature fields can be plotted in MATLAB, which can also calculate the flame length. Without soot modeling, flame length is instead determined by a threshold temperature, chosen as 1200 K, that defines a boundary for the flame. The flame length is defined as the difference between the minimum and maximum x -coordinates of the flame boundary.

3. Results and Discussion

The FIAT analysis of the top-view video created from the BASS still images provide the evolution of the flame leading edge, spread rate, flame length, and flame areas (total and yellow) with respect to time. This information is matched with radiometer and anemometer data printed on the frames of the side-view video to create the corresponding time profiles of radiation and opposed flow velocity. Since the flame spread rate can vary during the experiment (due to changes in opposed-flow velocity), the time profiles are converted to the relative location of the flame leading edges along the samples. Since the anemometer has a response time of approximately one minute [19], the flow velocity adjustments were matched with the astronauts' vocal confirmations recorded during the experiments, whereas no time delay was considered for the radiometer.

An example of radiometer values obtained from the experiment B6 (see Table 1) is given by the red squares in Fig. 3, which are read on the first frame of each second of the experimental video. These values are plotted along the sample, starting from the flame leading edge location when the igniter is turned off (see right pictures in Fig. 3). The total flame area was directly measured with FIAT area tracking, whereas the two-dimensional flame area was obtained by multiplying the flame length, independently measured with the intensity tracking method, by the sample width of 20 mm; in this way it is possible to compare flame length and area. The first rise of the radiometer signal is accompanied by the initial growth of the flame, as confirmed by the longer flames shown in the pictures of Fig. 4. The values of the forced flow velocity are indicated by the red line in the plot of Fig. 3, and the increase in flame length could be associated to the varying velocity gradient encountered by the flame while spreading along the sample [16]. The initial portion of the sample (0–40 mm) reflects the first 10–20 s of the experiment, and the increase of radiometer values could be due to the sensor response time (on the order of seconds) and the adjustment to the flame growth right after the fuel ignition. The position of the flame affects the solid angle described with the radiometer, but this effect could be compensated by an increase in radiative emission of fuel and surroundings that are heated up by the flame, and the increase of flame size. By looking at the interval between 40 mm and 70 mm, the radiometer values are quite stable around 34 mV, while the 2D flame area increases by about 120 mm^2 (corresponding to a variation of about 6 mm in flame length) and the measured area oscillates between 400 mm^2 and 600 mm^2 . Measured and 2D flame areas show good agreement with the increasing values of the radiometer throughout the experiment.

The three main parameters considered in this work are oxygen concentration, flow velocity and sample thickness. By selecting the experiments (or parts of them) where the ambient conditions are not varying (for at least 10 s), the radiometer signal (averaged over the time range with constant conditions) can be plotted as a function of each variable. For a better comparison, the averaged values are calculated when a flame is spreading over the central part of the sample; in this way changes in solid angles become minimal. Figure 4 shows the variation of experimental radiometer values (red symbols) with the three variables, with representa-

Table 1
BASS Experimental Matrix

	V_g (cm/s)	O ₂ (%)	Thickness (μ m)	Width (cm)	Radiometer (mV)
B1	5	22.2	100	2	25.72
B2	5	22.2	200	2	30.20
B3	1.5	22.2	100	2	19.77
B4	5	22.2	300	2	31.67
B5	4.5	22.2	200	2	28.45
B6	3.5	21	100	2	34.50
B7	1.5	22.2	400	2	25.03
B8	10	21	200	2	33.60
B8 (2)	42	21	200	2	24.17
B9	2	21	100	2	24.00
B10	2	21	200	1	13.57
B11	2	21	200	2	26.64
B12	1.5	22.2	300	2	23.37
B13	3	21	400	2	40.27
B14	–	15	200	1	No ignition
B15	10	21	100	2	43.67
B15 (2)	42	21	100	2	9.43
B16	1.5	17.3	100	2	9.12
B17	4	17.5	200	1	6.71
B18	10	17.4	200	1	9.20
B19	10	17.3	100	2	16.15
B20	3.5	17.4	100	2	11.40
B21	5.5	20.8	200	1	11.27
B22	1	20.7	200	1	3.83

The oxygen concentration was measured before the experiments, while flow velocity and radiometer values represent portions of experiments with constant burning conditions

tive flame pictures on the right of each plot. Radiation values from the numerical simulations are reported in the graphs as well (black symbols) but will be discussed later in this section. After an initial increase with flow velocity, flame radiation decreases with faster flows. The flame pictures show the initial growth sustained by higher velocities, as well as the final reduction in length and area, in accordance to the radiometer signal and expectations for the transition from radiative to kinetic regimes [14]. By keeping flow velocity and thickness constant and increasing oxygen concentration, the flame radiation shows a non-monotonic behavior, although the difference in radiometer values between 21% and 22% could be attributed to experimental uncertainties. The flame pictures show an increment in flame area when varying the oxygen from 17.4% to 22.2%, but the yellow region at 22.2% is actually smaller than at 21%. Although this could explain the experimental behavior of the radiometer, the number of data points are insufficient to confirm this trend. Finally, when oxygen concentration and flow velocity are constant (bottom graph of Fig. 5), radiometer values increase by about 20% when a thicker sample is burnt. The pictures show larger flame lengths for thicker fuels, but with smaller yellow regions. Direct visualization of the exper-

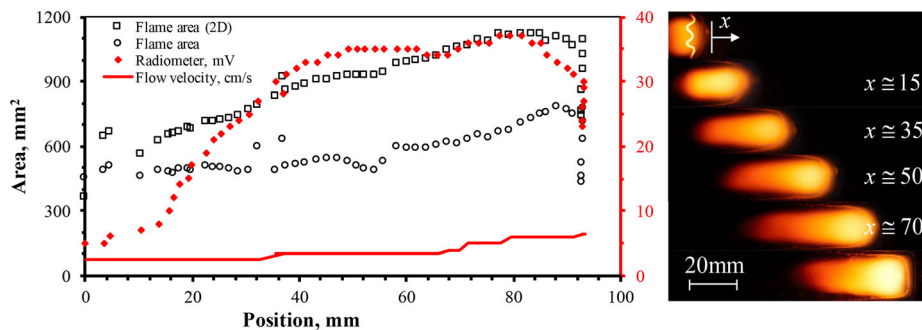


Figure 3. Radiometer and anemometer values read from the side video are shown in red corresponding to the right red axis for the flame spreading along the sample B6 (see Table 1). The graph also shows the variation of flame area measured with the FIAT area tracking, and two-dimensional area (obtained by multiplying flame length by sample width), with values associated to the black left axis. On the right, still-pictures show the flame evolution with time intervals of 10 s, with the corresponding x-position expressed in mm (Color figure online).

iments with 300 and 400 μm thick samples and their analysis suggest that these flames did not reach steady state in the limited experimental time and sample length.

The visualization of the pictures and radiometer values in Figs. 3 and 4 shows how changes in flame geometry and burning conditions affect flame strength and radiation. The experiments offer important information regarding flame geometry, which we characterize by tracking flame length and area of the yellow region. Meanwhile, numerical results can provide variable distributions such as temperature fields. Experimental and numerical results are compared qualitatively by considering the flame length. Figure 5 shows the evolution of simulated 2D flames (from a side view) with increasing flow velocity from 2 cm/s to 40 cm/s. The velocity values are similar to those of the experimental flames shown (from a top view) on the right of Fig. 5. When the forced flow was set to zero all the experimental flames extinguished within a few seconds, in agreement with the numerical results in a quiescent atmosphere with an oxygen concentration of 21%. The simulated temperature fields show a stronger flame with higher flow velocity, with the hottest region of the flame increasing in temperature. However, the length of the 1200 K flame boundary (indicated by the blue contours in the simulated flames in Fig. 5) first increases and then decreases, in the same way as the real flames. At 40 cm/s the flame gets closer to the solid surface and the hottest region shrinks significantly, as expected in the kinetic regime. The yellow regions on the right of Fig. 5 enlarge at higher velocities before shrinking again, and the increasing brightness suggests stronger flames. While a direct correlation between image color and temperature cannot be established, the similar trend between the experimental and numerical results enables comparison between the two.

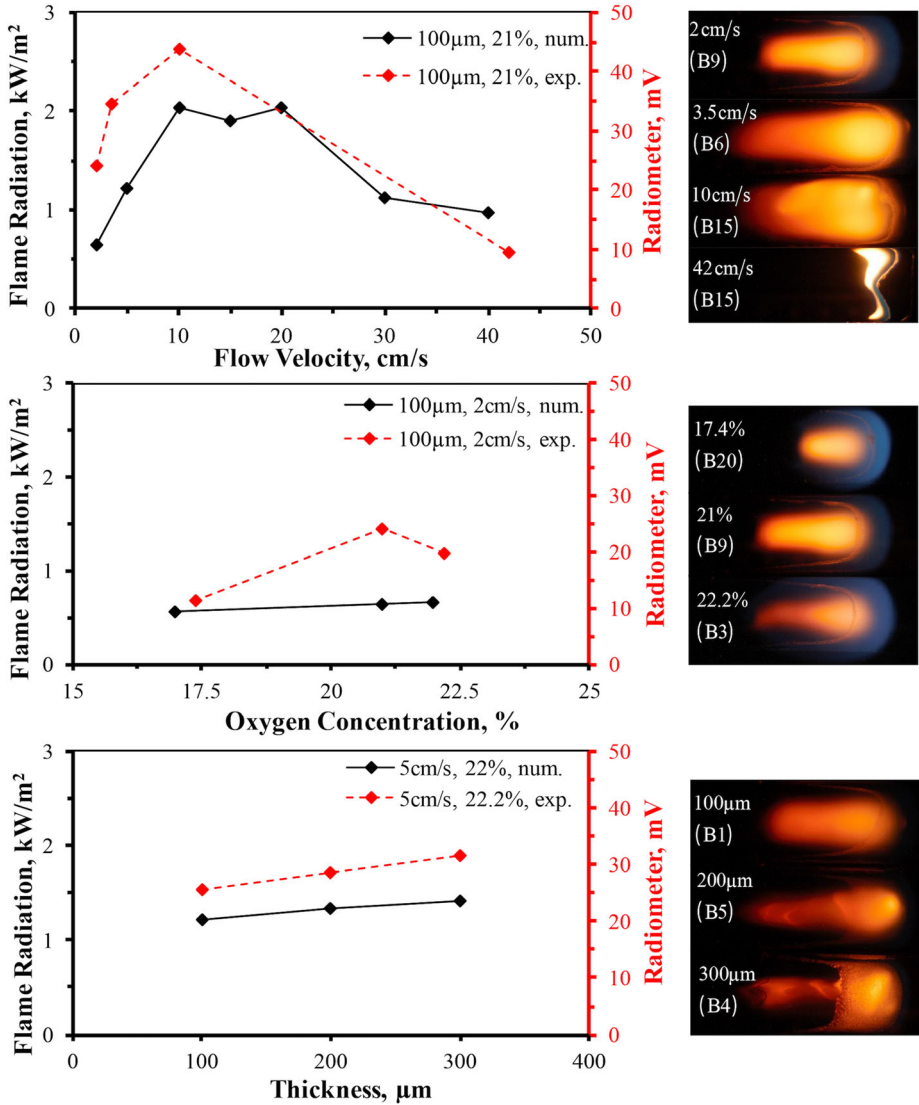


Figure 4. Radiometer signal read from the side videos (red symbols, dashed line) measured in mV, and from numerical simulations (black symbols, solid line). Flame radiation is plotted against flow velocity, oxygen concentration and thickness by isolating the experiments with two out of three variables being constant for at least 10 s (Color figure online).

The total radiation of a flame, with contribution from gas and solid phases, is calculated numerically via the RADCAL method at a point in space analogous to the radiometer position in the BASS tunnel (see Fig. 1). The variation of the radi-

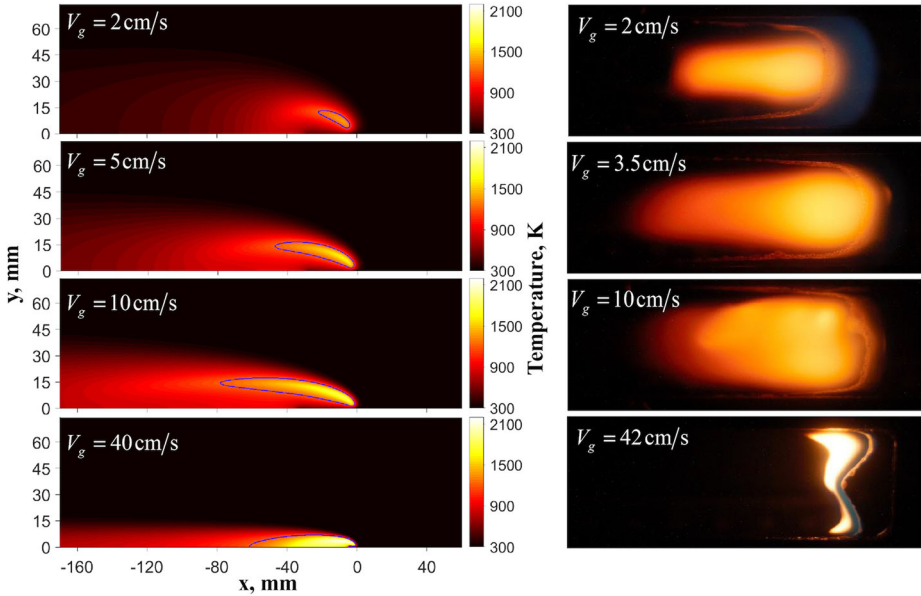


Figure 5. Comparison of simulated temperature fields (left) and top view of experimental flames (right) over 100 μm thick PMMA samples at 21% oxygen. The figure shows the effect of flow velocity on the temperature field inside of the domain and flame structure in the real flames.

ation per unit area is plotted in Fig. 4 to replicate the experimental conditions. When varying flow velocity, numerical radiation values follow the same trend as the experimental, although the curve presents a strange behavior between 10 cm/s and 20 cm/s. This oscillation is explained by the different maxima of gas and solid radiation, which do not occur at the same velocity. The increase in numerical radiation with oxygen concentration is mild with respect to the experimental values, whereas the thickness dependence has a similar slope to the radiometer values.

The fuel burning rate for given burning conditions is often used to estimate the total flame radiation. It was not directly measured in the BASS experiments, but it can be estimated by knowing the instantaneous flame spread rate and calculating the mass balance: $\dot{m} = \rho_s V_f 2\tau w$, where ρ_s is the PMMA density (1.19 g/cm^3), V_f is the flame spread rate, τ the fuel semi-thickness and w the sample width. The numerical model directly supplies the burning rates and, together with the experimental values, are plotted on the left graphs of Fig. 6 for the same range of burning conditions as in Fig. 4 (flow velocity, oxygen concentration and fuel thickness). On the third axis of the left graphs in Fig. 6 the numerical flame temperature is reported (defined as the highest temperature in the domain). Flow velocity has a similar effect on burning rates and radiative values in Fig. 4, despite the increase in flame temperature shown in the top graph of Fig. 6. Approaching

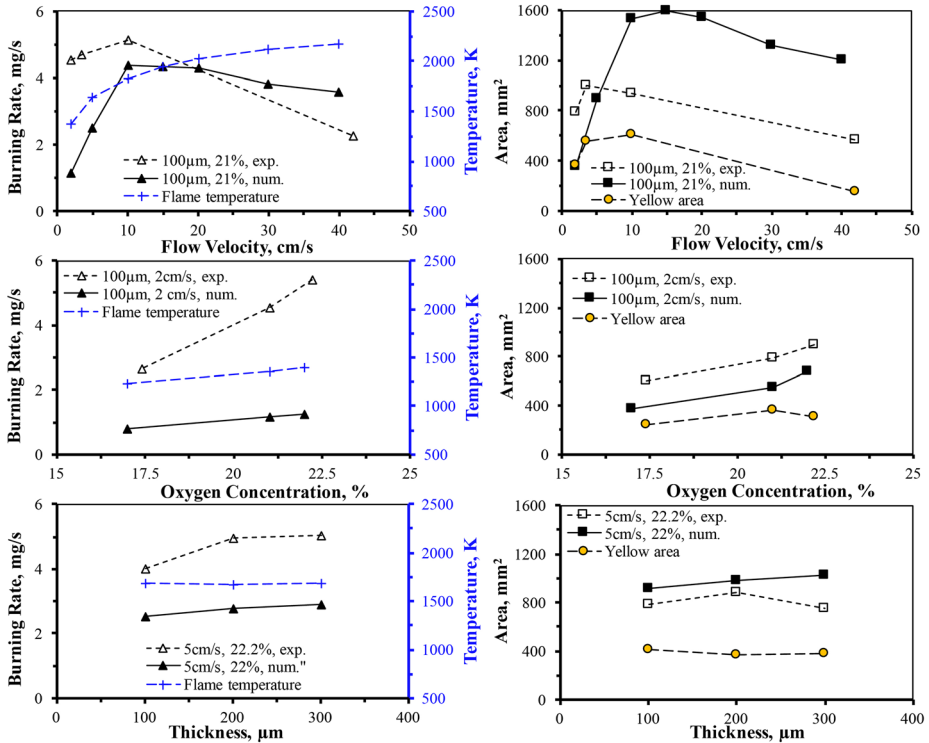


Figure 6. Parametric study of (left) burning rate and (right) flame area as function of flow velocity, oxygen concentration and fuel thickness. The numerical flame temperature is reported on the third axis of the left graphs.

the kinetic regime, in fact, radiative losses become less important, and the flame temperature increases asymptotically to the adiabatic value. However, the reduction in residence time causes the flame to shrink and slow down, with a consequent decrease in fuel burning rate. Numerical and experimental burning rates show the same trend despite the offset in values. Oxygen concentration is the variable in the second graph of Fig. 6 and, as expected, higher values are beneficial for both flame temperature and burning rates. The flame temperature does not depend on fuel thickness, as shown in the bottom graph of Fig. 6, because it is controlled by the gas phase. However, the burning rates and radiometer values increase with thickness in Fig. 4. Because of the different radiative contributions of soot content and flame temperature, the slower increase of the latter with respect to flame radiation at higher oxygen concentration and larger fuel thicknesses suggests that these flames produce more soot.

The graphs on the right of Fig. 6 show the same parametric study on yellow flame areas and total flame areas (obtained by multiplying flame length by sample width). Numerical values of flame length (obtained as described in Sect. 3) were multiplied by the sample width as well, and the calculated areas are indicated by

filled symbols. The trends of flame areas with the three variables are very similar to the burning rate trends, and the offset between numerical and experimental values reduces except for flow velocity. The similarity between burning rates and flame areas suggest that the latter, easy to measure, could be used to describe the radiative behavior of small flames. The abnormal reduction in radiometer output for higher oxygen concentration in Fig. 4 could be justified by the smaller yellow flame measured in Fig. 6, but looking at the bottom graphs showing the thickness dependence in Figs. 4 and 6 we can see that the yellow area does not completely agree with the radiative strength of a flame. Also, from Fig. 6 we can see that in the range of variables considered, the yellow regions are mostly affected by flow velocity, and secondly by oxygen concentration but not fuel thickness. It should be noticed, however, that flames burning over thicker samples require more time to reach steady-state, making the thickness effect difficult to establish from the experimental matrix of Table 1. This is also suggested by the videos, where values of radiometer, flame length and area tend to increase monotonically throughout the experiments in these cases.

4. Conclusions

The total hemispherical emission recorded by a radiometer from flames spreading over PMMA sheets facing a mild opposing flow of oxygen–nitrogen mixtures is reported in this work. Its variation with burning conditions is studied experimentally by isolating the effects of flow velocity, oxygen concentration and fuel thickness, and a comprehensive numerical model that includes gas and surface radiation with radiation feedback is used to understand the observed radiation characteristics. The numerical model reproduces in a qualitative manner the observed dependence of the flame shape and radiation signature on the parameters. Results show that higher flow velocities are beneficial for flame temperature and initially for the flame size, but the flames shrink at higher velocities causing the radiative emission to drop. This is consistent with the kinetic regime assumption that radiation becomes less important when the residence time decreases (although flame temperature increases). The experimental data to describe the effect of oxygen concentration are not enough to establish a trend, but they suggest that soot production might play a bigger role than flame temperature with increasing oxygen levels, due to the lower increment of the numerical flame temperature (about 15%) with respect to flame radiation (about 20% numerically and 70% experimentally) in the same range of oxygen concentrations. The total flame area does not change significantly with fuel thickness, and the increase in radiation is attributed to a larger emission from the pyrolysis region (which becomes longer for thicker fuels). Fuel burning rates, calculated from the instantaneous flame spread rate in the experiments and compared to the simulated values, are shown to correlate well with the radiation signatures. Measurements of total and yellow areas, however, show similar trends for total radiation, and are supported by the numerical results. This agreement suggests that soot, which is not included in the numerical model, might play a smaller role in the radiative emission of a

flame over solid fuels rather than from gaseous fuels because of the strong influence of surface radiation. Further studies are needed to prove this conclusion and understanding the driving radiation losses and gains between flame and fuel. Understanding the most influential burning conditions on flame radiative heat transfer in reduced gravity is necessary to improve fire safety onboard spacecraft, and their estimations from indirect measurements such as flame area projection would be beneficial due to the very limited number of available experiments.

Acknowledgements

This work was funded by the NASA ISS Research Project Office with Dr. David Urban serving as the contract monitor. The authors would also like to thank Dr. Sandra Olson from NASA Glenn Center for the constructive conversations.

References

1. Wichman I (1992) Theory of opposed-flow flame spread. *Prog Energy Combust Sci* 18:646–651
2. Williams F (1977) Mechanisms of fire spread. In: *Symposium (international) combustion*, vol 16. pp 1281–1294
3. Bhattacharjee S, Laue M, Carmignani L, Ferkul P, Olson S (2016) Opposed-flow flame spread: a comparison of microgravity and normal gravity experiments to establish the thermal regime. *Fire Saf J* 79:111–118
4. Fernandez-Pello A, Hirano T (1983) Controlling mechanisms of flame spread. *Combust Sci Technol* 32:1–31
5. Bhattacharjee S, Altenkirch RA (1990) Radiation-controlled, opposed-flow flame spread in a microgravity environment. In: *Symposium (international) combustion* vol 23. pp 1627–1633
6. Fernandez-Pello A, Ray S, Glassman I (1981) Flame spread in an opposed forced flow: the effect of ambient oxygen concentration. In: *Symposium (international) combustion*, vol 18. pp 579–589
7. Zhao K, Zhou X, Liu X, Tang W, Gollner M, Peng F, Yang L (2018) Experimental and theoretical study on downward flame spread over uninhibited PMMA slabs under different pressure environments. *Appl Therm Eng* 136:1–8
8. Bhattacharjee S, Altenkirch R (1992) A comparison of theoretical and experimental results in flame spread over thin condensed fuels in quiescent, microgravity environment. In: *Symposium (international) combustion* vol 24. pp 1669–1676
9. Ramachandra P, Altenkirch R, Bhattacharjee S, Tang L, Sacksteder K, Wolverton M (1995) The behavior of flames spreading over thin solids in microgravity. *Combust Flame* 100:71–84
10. Altenkirch RA, Bundy MF, Tang L, Bhattacharjee S, Sacksteder K, Delichatsios MA (1999) Reflight of the solid surface combustion experiment: flame radiation near extinction. In: *5th International microgravity combusting workshop*, Cleveland
11. West J, Tang L, Altenkirch R, Bhattacharjee S, Sacksteder K, Delichatsios M (1996) Quiescent flame spread over thick fuels in microgravity. In: *Symposium (international) combustion* vol 26. pp 1335–1343

12. Haynes B, Wagner H (1981) Soot formation. *Prog Energy Combust Sci* 7:229–273
13. Glassman I (1988) Soot formation in combustion process. In: *Symposium (international) combustion*, vol 22. pp 295–311
14. Bhattacharjee S, Simsek A, Miller F, Olson S, Ferkul P (2017) Radiative, thermal, and kinetic regimes of opposed-flow flame spread: a comparison between experiment and theory. *Proc Combust Inst* 36:2963–2969
15. Bhattacharjee S, Simsek A, Olson S, Ferkul P (2016) The critical flow velocity for radiative extinction in opposed-flow flame spread in a microgravity environment: a comparison of experimental, computational, and theoretical results. *Combust Flame* 163:472–477
16. Carmignani L, Bhattacharjee S, Olson SL, Ferkul PV (2018) Boundary layer effect on opposed-flow flame spread and flame length over thin PMMA in microgravity. *Combust Sci Technol* 190:534–548
17. Urban D, Ferkul P, Olson S, Ruff G, Easton J, T'ien J, Liao Y-T, Li C, Fernandez-Pello C, Torero J, Legros G, Eigenbrod C, Smirnov N, Fujita O, Rouvreau S, Toth B, Jomaas G (2019) Flame spread: effects of microgravity and scale. *Combust Flame* 199:168–182
18. Olson S, Ferkul P (2017) Microgravity flammability boundary for PMMA rods in axial stagnation flow: experimental results and energy balance analyses. *Combust Flame* 180:217–229
19. Olson S, Ferkul P, Bhattacharjee S, Miller F, Fernandez-Pello A, Link S, T'ien J, Wichman I (2015) Results from on-board CSA-CP and CDM sensor readings during the burning and suppression of solids – II (BASS-II) experiment in the microgravity science glovebox (MSG). In: *45th ICES*, Bellevue, Washington
20. Bhattacharjee S, Carmignani L, Celniker G, Rhoades B (2017) Measurement of instantaneous flame spread rate over solid fuels using image analysis. *Fire Saf J* 91:123–129
21. Bhattacharjee S, Nagarkar R, Nakamura Y (2014) A Correlation for an effective flow velocity for capturing the boundary layer effect in opposed-flow flame spread over thin fuels. *Combust Sci Technol* 186:975–987
22. Grosshandler W (1993) A narrow-band model for radiation calculations in a combustion environment. *NIST Technical Note* 1402
23. Bhattacharjee S, Paolini C, Miller F, Nagarkar R (2012) Radiation signature in opposed-flow flame spread. *Prog. Computational Fluid Dynamics* 12:293–301